ON THE LIMB DARKENING, SPECTRAL ENERGY DISTRIBUTION, AND TEMPERATURE STRUCTURE OF PROCYON

J. P. AUFDENBERG[1]

National Optical Astronomy Observatory, 950 North Cherry Avenue, Tucson, AZ 85719

H.-G. LUDWIG

Lund Observatory, Lund University, Box 43, 22100 Lund, Sweden

AND

P. KERVELLA

LESIA, UMR 8109, Observatoire de Paris-Meudon, 5 place Jules Janssen, 92195 Meudon Cedex, France

ABSTRACT

We have fit synthetic visibilities from three-dimensional (CO^{5}BOLD+PHOENIX) and one-dimensional (PHOENIX, ATLAS 12) model stellar atmospheres of Procyon (F5 IV) to high-precision interferometric data from the VLT Interferometer (*K* band) and from the Mark III interferometer (500 and 800 nm). These data sets provide a test of theoretical wavelength-dependent limb-darkening predictions. The work of Allende Prieto et al. has shown that the temperature structure from a spatially and temporally averaged three-dimensional hydrodynamic model produces significantly less limb darkening at 500 nm relative to the temperature structure of a one-dimensional MARCS model atmosphere with a standard mixing-length approximation for convection. Our direct fits to the interferometric data confirm this prediction. A one-dimensional ATLAS 12 model with "approximate overshooting" provides the required temperature gradient. We show, however, that one-dimensional models cannot reproduce the ultraviolet spectrophotometry below 160 nm with effective temperatures in the range constrained by the measured bolometric flux and angular diameter. We find that a good match to the full spectral energy distribution can be obtained with a composite model consisting of a weighted average of 12 one-dimensional model atmospheres based on the surface intensity distribution of a three-dimensional granulation simulation. We emphasize that one-dimensional models with overshooting may realistically represent the mean temperature structure of F-type stars such as Procyon, but the same models will predict redder colors than observed because they lack the multicomponent temperature distribution expected for the surfaces of these stars.

Subject headings: convection — methods: numerical — stars: atmospheres — stars: fundamental parameters (colors, temperatures) — stars: individual (Procyon) — techniques: interferometric

1. INTRODUCTION

The connection between the transport of energy in stellar atmospheres and the limb darkening (LD) of stellar photospheres has been under investigation for nearly 100 years in the case of the Sun. Since the work of Schwarzschild (1906), the darkening of the solar limb has been investigated to understand the roles of convection and radiation in the transport of energy through the Sun's atmosphere. Assuming that the mass absorption coefficient of the solar atmosphere was both wavelength and depth independent and that the angle-dependent intensity could be replaced by the mean intensity at each depth, Schwarzschild derived a center-to-limb intensity variation based on a purely radiative equilibrium temperature structure:

$$\frac{I(\tau = 0, \ \cos\theta)}{I(0, \ 1)} = 1 - \beta(1 - \cos\theta), \quad \beta = \frac{2}{3}, \quad (1)$$

where τ is the optical depth, θ is the angle between the line of sight and the emergent intensity, and β is the linear LD coefficient. Schwarzschild showed this LD law to be more consistent with contemporary observations than an LD law based on an

adiabatic equilibrium temperature structure. Milne (1921) improved on Schwarzschild's mean intensity approximation and found that a radiative equilibrium temperature structure with improved flux conservation yielded an LD coefficient of $\beta = \frac{3}{5}$, in better agreement with observations.

The studies of Schwarzschild and Milne were completed before hydrogen was recognized as the principal constituent of the Sun's atmosphere by Payne (1925), before the work of Unsöld (1930) concerning the effects of hydrogen ionization on the stability of radiative equilibrium against convection, and before the importance of the bound-free and free-free opacity of the negative ion of hydrogen was recognized by Wildt (1939). Plaskett (1936) inverted solar LD observations to find a temperature structure inconsistent with radiative equilibrium, suggesting that convection has a significant effect on LD. Keenan (1938) showed that this conclusion was acceptable only if the adiabatic gradient began at optical depths considerably less than $\bar{\tau} \sim 2$, contrary to Unsöld's calculations. The reasoning was that convection currents should transport little energy above the zone of instability and that radiative equilibrium should prevail at smaller optical depths significant to LD. Plaskett's conclusion was further critiqued by Woolley (1941), who showed that it necessitates convective velocities large enough to blur the Fraunhofer lines. Woolley attributed the differences between the observations and

[1] Michelson Postdoctoral Fellow.

the radiative equilibrium models to the frequency-dependent opacity of the solar atmosphere, not yet included in the models. As model atmospheres were improved with the incorporation of line blanketing and mixing-length convection, subsequent studies (Münch 1945; Swihart 1956; Spiegel 1963; Travis & Matsushima 1973; Vernazza et al. 1976; Koutchmy et al. 1977) generally confirmed Woolley's suggestion and concluded that the effects of convection on LD were subtle or insignificant. Recently, Castelli et al. (1997) have shown that an "approximate overshooting" modification to the standard one-dimensional mixing-length convection treatment enhances convective transport at smaller optical depths and provides a better fit to solar LD observations than models without overshooting. Overshooting refers to the depth of convective penetration into layers of the atmosphere stable against convection under the Schwarzschild criterion.

Photospheric convection and LD are again the focus of some of the most exciting observational and theoretical studies in astrophysics. Recently, space-based photometric observations (Matthews et al. 2004) have put an upper limit on pressure-mode oscillations excited by turbulent convection in the atmosphere of the F-subgiant Procyon. Precise ground-based photometric microlensing observations are providing multiband LD measurements of solar-like stars (Abe et al. 2003), and recent observations of this kind are challenging model LD predictions for cool giants (Fields et al. 2003). Increasingly precise long-baseline interferometric measurements at optical and near-infrared wavelengths (Wittkowski et al. 2004; Ohishi et al. 2004; Perrin et al. 2004) are providing new tests of LD predictions. Tests of these predictions are important because they aid not only in the interpretation of interferometric data, but in the studies of eclipsing binaries, transiting extrasolar planets, and their host stars.

Along with these recent observational developments, three-dimensional, time-dependent radiation hydrodynamic simulations (Stein & Nordlund 1998; Robinson et al. 2003) have been produced to study solar granulation. With the aid of such models, the study of spectral line formation in solar granulation (Asplund et al. 2004) has recently significantly revised the solar elemental oxygen abundance. These simulations model in great detail the transition from convection-dominated transport to radiation-dominated transport near the surface of the solar atmosphere. Self-consistent, and not employing the usual one-dimensional mixing-length theory, these simulations predict a spatially and temporally averaged temperature profile for the solar atmosphere that samples upflows and downdrafts across the model solar surface. Similar models have also been developed for cooler and more evolved stars (e.g., Freytag et al. 2002; Ludwig et al. 2002; Robinson et al. 2004). For the Sun, multiwavelength LD observations are used to test the *intensities* predicted by these models, in addition to spectroscopic tests of the *flux* predictions. Qualitatively, multiwavelength solar LD predictions from three-dimensional models (Asplund et al. 1999, Fig. 3) and one-dimensional models with overshooting (Castelli et al. 1997, Fig. 4) are in reasonable agreement with the observations of Neckel & Labs (1994). Both these studies find that standard one-dimensional mixing-length theory predicts LD that is too strong, most noticeably in the blue (500 nm). A similar relationship between three-dimensional and one-dimensional LD predictions has been established for Procyon (Allende Prieto et al. 2002, hereafter AP02). These predictions for Procyon have until now not been directly tested by long-baseline interferometric observations, and this is the principal motivation for this paper.

Procyon (α CMi, HR 2943, HD 61421), an F-type subgiant (F5 IV–V; Gray et al. 2001) with a white dwarf companion, has

been a prime target for both observational and theoretical asteroseismological studies (Martić et al. 1999; Chaboyer et al. 1999) because its visual orbital solution and measured angular diameter provide well-constrained estimates of its fundamental stellar parameters: effective temperature, gravity, radius, and mass, most recently improved upon by Girard et al. (2000) and Kervella et al. (2004b). The model of AP02 reproduces spectral line shifts, signatures of convective motion, measured from very high resolution ($R \simeq 200,000$) spectroscopy of Procyon. A comparison between this three-dimensional model and a homogeneous, hydrostatic one-dimensional model atmosphere from the MARCS code (Asplund et al. 1997; Gustafsson et al. 1975), with mixing-length convection and the same effective temperature and gravity, shows that at 1 μm the normalized center-to-limb predictions are quite comparable while at 450 nm the one-dimensional intensity profile is up to 20% fainter than the three-dimensional intensity profile at intermediate limb angles. This LD contrast can be quantified with respect to interferometric observations by comparing the predicted LD corrections for the two models. The LD correction is a model-dependent scale factor between the angular size derived from the visibility data assuming a uniformly bright stellar disk and the true wavelength-independent angular size corresponding to a physical radius (see, e.g., Davis et al. 2000). From AP02, the monochromatic LD corrections at 450 nm are 1.081 (one-dimensional model) and 1.064 (three-dimensional model), a difference of 1.6%. In this paper we test this prediction by comparing both one-dimensional and three-dimensional models directly with precise interferometric visibility measurements obtained in two intermediate bands at 500 and 800 nm, and in the K band at 2.2 μm.

It is also interesting to compare the uncertainty in a typical interferometric effective temperature estimate ($\simeq$100–200 K) with the horizontal temperature variation expected from three-dimensional models. The AP02 three-dimensional model for Procyon shows an rms spatial temperature variation of ~500 K (8%) at a depth defined by a Rosseland optical depth of unity. As a result, while the bolometric flux and the angular diameter provide a temperature that represents the bolometric output of the photosphere, a one-dimensional atmosphere with this temperature is not expected to accurately represent the spectral energy distribution (SED). For this reason, in addition to testing the three-dimensional model LD predictions, we also compare predictions of a three-dimensional model atmosphere to archival spectrophotometry and Strömgren photometry.

The broad wavelength coverage needed for the interferometric test requires data from more than one interferometer. We use 500 and 800 nm data from the Mark III interferometer (Shao et al. 1988) and 2.2 μm data from the Very Large Telescope Interferometer (VLTI), specifically its commissioning instrument VINCI (Kervella et al. 2004a). In § 2 we describe the observations and present the observational data, and in § 3 we describe the model atmospheres and the computation of the synthetic visibilities and the synthetic spectrophotometry. In § 4 we show the comparison of the synthetic visibilities computed from the model atmospheres with the visibility data and archival photometric data. These results are discussed in § 5 and briefly summarized in § 6.

2. OBSERVATIONS AND FUNDAMENTAL PARAMETERS

2.1. *Interferometric Observations*

2.1.1. *VLTI Observations*

The European Southern Observatory's VLTI (Glindemann et al. 2003) has been operated on top of the Cerro Paranal in

TABLE 1
VLTI VINCI K-BAND VISIBILITY MEASUREMENTS

Julian Date	Projected Baseline (m)	Position Angle (deg)	$V^2 \times 100$	$\sigma V_{stat}^2 \times 100$	$\sigma V_{sys}^2 \times 100$	$\sigma V_{total}^2 \times 100$	Calibration Star
2,452,674.59969..............	21.900	73.45	83.01	1.90	0.12	1.90	α CMa
2,452,674.60482..............	22.192	73.51	83.50	2.20	0.12	2.21	α CMa
2,452,674.60889..............	22.409	73.54	83.76	2.18	0.12	2.18	α CMa
2,452,672.72358..............	23.005	70.29	81.90	1.31	0.08	1.31	α CMa
2,452,682.69435..............	23.081	70.42	86.17	3.20	0.07	3.20	α CMa
2,452,685.68579..............	23.095	70.45	84.07	1.86	0.08	1.86	α CMa
2,452,671.72379..............	23.104	70.46	84.09	3.61	0.07	3.61	α CMa
2,452,681.69611..............	23.118	70.49	84.93	3.86	0.08	3.87	α CMa
2,452,672.72041..............	23.129	70.50	83.48	1.13	0.08	1.14	α CMa
2,452,683.68954..............	23.160	70.56	84.70	2.88	0.09	2.88	α CMa
2,452,682.69041..............	23.227	70.68	83.64	3.12	0.07	3.12	α CMa
2,452,681.69192..............	23.271	70.76	83.88	3.81	0.08	3.81	α CMa
2,452,679.69711..............	23.280	70.77	81.32	3.88	0.23	3.89	α CMa
2,452,671.71859..............	23.293	70.80	82.83	3.40	0.07	3.40	α CMa
2,452,683.68469..............	23.331	70.87	82.44	2.73	0.09	2.73	α CMa
2,452,682.68572..............	23.386	70.97	80.90	3.01	0.07	3.01	α CMa
2,452,679.69316..............	23.410	71.01	83.33	2.38	0.23	2.39	α CMa
2,452,671.71484..............	23.415	71.02	82.49	2.19	0.07	2.20	α CMa
2,452,683.68116..............	23.443	71.08	82.54	2.71	0.09	2.71	α CMa
2,452,671.70658..............	23.644	71.48	80.91	2.43	0.07	2.43	α CMa
2,452,671.70225..............	23.741	71.71	81.93	2.43	0.07	2.43	α CMa
2,452,684.66566..............	23.764	71.76	83.54	2.51	0.09	2.51	α CMa
2,452,685.66048..............	23.810	71.88	83.32	1.83	0.09	1.84	α CMa
2,452,684.62226..............	23.819	73.24	80.76	2.43	0.08	2.43	α CMa
2,452,671.69791..............	23.824	71.91	85.10	2.57	0.07	2.57	α CMa
2,452,684.66129..............	23.842	71.96	82.11	2.47	0.08	2.47	α CMa
2,452,685.65611..............	23.879	72.07	82.65	1.71	0.09	1.72	α CMa
2,452,683.62916..............	23.884	73.15	82.34	2.74	0.09	2.74	α CMa
2,452,684.62693..............	23.891	73.14	84.20	2.66	0.09	2.66	α CMa
2,452,682.66269..............	23.901	72.15	80.19	2.99	0.07	2.99	α CMa
2,452,684.65703..............	23.903	72.15	82.22	2.47	0.08	2.47	α CMa
2,452,671.69151..............	23.915	72.20	82.27	2.16	0.07	2.16	α CMa
2,452,685.65156..............	23.934	72.27	80.65	1.68	0.09	1.68	α CMa
2,452,683.63367..............	23.938	73.04	82.01	2.76	0.09	2.76	α CMa
2,452,684.63099..............	23.938	73.04	80.15	2.72	0.08	2.72	α CMa
2,452,682.65863..............	23.945	72.31	82.83	3.08	0.07	3.08	α CMa
2,452,672.68439..............	23.958	72.37	81.00	1.13	0.08	1.13	α CMa
2,452,674.67842..............	23.962	72.39	81.05	1.80	0.10	1.81	α CMa
2,452,683.65385..............	23.962	72.39	83.33	2.78	0.09	2.78	α CMa
2,452,683.63773..............	23.971	72.93	81.89	2.80	0.09	2.80	α CMa
2,452,682.65360..............	23.981	72.50	80.45	3.00	0.07	3.00	α CMa
2,452,684.64797..............	23.981	72.51	82.02	2.47	0.08	2.48	α CMa
2,452,685.63493..............	23.985	72.85	82.08	1.94	0.09	1.94	α CMa
2,452,683.64960..............	23.986	72.55	83.19	2.78	0.09	2.78	α CMa
2,452,674.67396..............	23.987	72.56	81.92	1.82	0.10	1.82	α CMa
2,452,672.67922..............	23.988	72.56	79.78	1.16	0.08	1.16	α CMa
2,452,685.64373..............	23.988	72.56	79.08	1.91	0.08	1.91	α CMa
2,452,684.63971..............	23.991	72.79	81.00	2.43	0.08	2.44	α CMa
2,452,684.64410..............	23.993	72.65	81.56	2.45	0.08	2.45	α CMa
2,452,672.67394..............	23.994	72.74	80.85	1.10	0.08	1.10	α CMa
2,452,674.67012..............	23.995	72.69	81.18	1.80	0.10	1.80	α CMa
2,452,683.64541..............	23.995	72.69	81.71	2.72	0.09	2.72	α CMa
2,452,685.63998..............	23.995	72.69	79.22	1.68	0.08	1.68	α CMa
2,453,002.63052..............	42.518	69.88	54.52	1.23	0.22	1.25	30 Gem
2,453,002.63564..............	43.943	70.39	51.89	1.16	0.21	1.18	30 Gem
2,453,002.66192..............	50.648	72.27	40.22	0.51	0.18	0.54	30 Gem
2,453,002.66734..............	51.889	72.53	36.85	0.71	0.16	0.73	30 Gem
2,452,339.59761..............	55.734	147.99	32.92	1.33	0.44	1.40	α CMa
2,452,339.59331..............	56.237	147.32	29.39	0.99	0.40	1.07	α CMa
2,452,339.58907..............	56.731	146.69	31.28	1.11	0.42	1.18	α CMa
2,453,002.69427..............	57.239	73.37	28.79	0.50	0.13	0.52	30 Gem
2,453,029.62077..............	57.277	73.37	29.14	2.01	0.10	2.02	18 Mon
2,453,002.69950..............	58.111	73.45	27.98	0.48	0.13	0.50	30 Gem

TABLE 1—*Continued*

Julian Date	Projected Baseline (m)	Position Angle (deg)	$V^2 \times 100$	$\sigma V^2_{stat} \times 100$	$\sigma V^2_{sys} \times 100$	$\sigma V^2_{total} \times 100$	Calibration Star
2,453,029.62595..................	58.137	73.45	27.79	1.92	0.10	1.92	18 Mon
2,452,994.73707..................	60.383	73.58	25.89	0.45	0.15	0.47	HR 1799
2,453,002.72628..................	61.657	73.57	22.37	0.73	0.09	0.73	18 Mon
2,453,002.73158..................	62.172	73.54	22.10	1.05	0.09	1.06	18 Mon
2,452,996.75146..................	62.477	73.51	22.06	0.25	0.08	0.27	6 Leo
2,452,996.75644..................	62.863	73.45	21.48	0.26	0.08	0.27	6 Leo
2,452,995.76035..................	62.946	73.43	21.06	0.33	0.08	0.34	6 Leo
2,452,996.81799..................	62.952	71.42	21.44	0.33	0.11	0.34	6 Leo
2,452,995.81464..................	63.326	71.74	20.80	0.27	0.10	0.28	6 Leo
2,452,996.81167..................	63.339	71.75	20.41	0.27	0.10	0.29	6 Leo
2,452,995.80179..................	63.845	72.31	20.26	0.27	0.10	0.29	6 Leo
2,452,996.78120..................	63.942	72.93	19.80	0.18	0.08	0.20	6 Leo
2,453,002.76593..................	63.957	72.89	20.05	0.59	0.08	0.60	18 Mon
2,452,996.78597..................	63.988	72.78	19.85	0.20	0.08	0.22	6 Leo
2,453,002.77184..................	63.991	72.71	19.88	0.66	0.08	0.66	18 Mon

northern Chile since 2001 March. The new observations presented in this paper were obtained by combining coherently the light coming from the two VLTI test siderostats (0.35 m aperture) on the E0–G1 baseline of the VLTI (66 m in ground length).

We used the VINCI beam combiner (Kervella et al. 2003b) equipped with a regular *K*-band filter ($\lambda = 2.0–2.4\ \mu$m). While the observations presented by Kervella et al. (2004b) were limited to a maximum baseline of 24 m, the 22 new squared visibility measurements cover the 42–66 m range, significantly lower in the first lobe of the Procyon visibility curve. Both the 24 and 66 m baseline data are listed in Table 1.

The raw data were processed using a wavelet-based algorithm (Kervella et al. 2004a) to obtain the instrumental squared moduli of the coherence factors. The instrumental transfer function was deduced from observations of four calibrator stars (HR 1799, 6 Leo, 18 Mon, and 30 Gem) whose a priori angular diameters were taken from the Cohen et al. (1999) list. Their linear LD coefficients were taken from Claret (2000) tables for the *K* band. The 24 m baseline data previously published in Kervella et al. (2004b), as well as three points from the 66 m baseline, were calibrated using Sirius as the reference star. Its well-determined angular diameter (Kervella et al. 2003a) results in a small systematic uncertainty on the calibrated visibilities of Procyon. Furthermore, the Sirius-calibrated visibilities obtained on the longer E0–G1 baseline show no detectable deviation from the other calibrators. The other calibrators have small angular diameters compared to Procyon (≈ 2 mas vs. more than 5 mas). This translates into small systematic errors on the calibrated visibility data. These errors were carried through the data reduction process and are reported in Table 1, together with the associated calibrator stars.

Apart from Sirius, the calibrators of the VLTI VINCI data are all K giants from the list established by Cohen et al. (1999). For this homogeneous set of stars, the limb-darkening correction LD/UD (uniform disk) is always in the 1.02–1.03 range. The LD correction for Procyon in the *K* band being just below LD/UD = 1.02, it is almost identical, and this correction cancels out. For Sirius, the effective temperature is higher ($\sim$10,000 K), resulting in a smaller LD correction of 1.012. In order to take into account properly this 0.7% difference, we have used the linear LD correction from Claret (2000). Considering the small amplitude of this correction (1.2%), the introduced systematic uncertainty is considered negligible compared to the VINCI error bar

on the best-estimate LD angular diameter of Procyon, 5.404 ± 0.031 mas, ±0.6% (see § 4). The infrared *K* band is an advantage in this matter, as the LD corrections are small and do not change much over a broad range of effective temperatures.

2.1.2. *Mark III Observations*

The Mark III interferometric data presented here comprise visibility measurements at 800 nm (Mozurkewich et al. 1991, Fig. 1*i*) from which uniform disk angular diameter fits have already been published (Mozurkewich et al. 1991, 2003) and unpublished visibility measurements at 500 nm from D. Mozurkewich (2004, private communication). We list these data in Tables 2 and 3 so that others may fit models directly to these visibilities. Mozurkewich et al. (1991, 2003) do not provide a listing of calibrator stars. They note, however, that the calibrator stars are all smaller than the program stars, and we expect the calibrator visibilities to be largely insensitive to model-dependent systematic uncertainties due to LD. Seriously large systematic errors seem to be ruled out by a comparison of the published Mark III uniform-disk fits at 450 nm to the earlier Intensity Interferometer uniform-disk fits at 443 nm (Hanbury Brown et al. 1974), which agree within 1 σ.

2.2. *Initial Fundamental Parameters*

2.2.1. *Effective Temperature*

Fundamental stellar parameters for Procyon are well constrained by direct measures of its bolometric flux and angular diameter. The bolometric flux is derived from an integration of Procyon's SED. Absolute spectrophotometry in the ultraviolet comes from the *International Ultraviolet Explorer* (low-dispersion, large-aperture spectra SWP43428 and LWR09108 from the *IUE* Newly Extracted Spectra archive [Rodríguez-Pascual et al. 1999], effectively from 170 to 306 nm) and from the *Hubble Space Telescope* Space Telescope Imaging Spectrograph (STIS; 10 one-dimensional extracted spectra in the sequence o6l501020 to o6l5010k0 from 220 to 410 nm). For integration, the ultraviolet data are binned to 1 nm resolution. Absolute spectrophotometry in the visual and near-infrared wavelength range (322.5–1027.5 nm, 5 nm resolution) has been obtained by Glushneva et al. (1992). For the SED beyond 1 μm, the broadband photometry (*JHKLMN*) from Morel & Magnenat (1978), with the absolute calibration of Johnson (1965) for *JKLMN* and Bessell & Brett (1988) for *H*, is fit using

TABLE 2
Mark III 500 nm Visibility Measurements

Julian Date	Projected Baseline (m)	Position Angle (deg)	V^2	$\sigma V^2_{\text{total}}$
2,447,452.956	2.803	23.049	1.024	0.106
2,447,452.970	2.768	20.864	0.900	0.089
2,447,452.986	2.728	17.918	0.944	0.072
2,447,453.004	2.689	14.543	0.966	0.073
2,447,453.041	2.630	6.448	1.013	0.075
2,447,453.924	2.877	27.258	0.859	0.058
2,447,453.936	2.847	25.646	0.911	0.049
2,447,453.949	2.814	23.750	0.984	0.051
2,447,453.962	2.781	21.688	0.904	0.046
2,447,453.981	2.734	18.425	0.940	0.048
2,447,454.921	5.093	27.288	0.894	0.053
2,447,454.957	4.934	22.135	0.780	0.046
2,447,454.969	4.878	20.047	0.804	0.048
2,447,454.980	4.833	18.154	0.884	0.051
2,447,454.993	4.778	15.552	0.933	0.054
2,447,455.003	4.741	13.490	0.925	0.054
2,447,455.015	4.705	11.116	0.927	0.054
2,447,455.024	4.680	9.063	0.954	0.055
2,447,455.037	4.653	6.184	0.831	0.051
2,447,455.050	4.636	3.183	0.893	0.052
2,447,455.910	6.686	28.266	0.578	0.048
2,447,455.928	6.587	25.979	0.730	0.057
2,447,455.945	6.490	23.593	0.659	0.052
2,447,455.962	6.384	20.683	0.762	0.059
2,447,455.974	6.319	18.661	0.694	0.053
2,447,455.985	6.258	16.546	0.755	0.057
2,447,455.996	6.204	14.363	0.802	0.061
2,447,456.007	6.155	12.079	0.828	0.063
2,447,456.018	6.114	9.724	0.836	0.064
2,447,456.030	6.079	7.157	0.826	0.063
2,447,456.041	6.055	4.478	0.800	0.061
2,447,456.916	22.193	27.143	0.010	0.002
2,447,456.935	21.836	24.598	0.016	0.003
2,447,457.046	20.215	2.793	0.035	0.009
2,447,457.964	21.220	19.514	0.020	0.002
2,447,457.976	20.984	17.152	0.024	0.003
2,447,457.993	20.703	13.805	0.031	0.002
2,447,458.008	20.505	10.815	0.030	0.002
2,447,458.019	20.377	8.311	0.032	0.002
2,447,458.034	20.256	4.843	0.033	0.002
2,447,458.044	20.213	2.678	0.038	0.002
2,447,458.053	20.195	0.435	0.040	0.002
2,447,460.952	29.068	20.149	0.006	0.002
2,447,460.970	28.613	16.858	0.003	0.002

TABLE 3
Mark III 800 nm Visibility Measurements

Julian Date	Projected Baseline (m)	Position Angle (deg)	V^2	$\sigma V^2_{\text{total}}$
2,447,452.956	2.803	23.048	1.016	0.049
2,447,452.970	2.768	20.863	0.948	0.043
2,447,452.986	2.728	17.918	1.009	0.037
2,447,453.004	2.689	14.544	0.988	0.035
2,447,453.022	2.656	10.718	0.997	0.035
2,447,453.041	2.630	6.447	1.015	0.036
2,447,453.924	2.877	27.260	0.964	0.042
2,447,453.936	2.847	25.647	0.968	0.029
2,447,453.949	2.814	23.750	1.003	0.030
2,447,453.962	2.781	21.688	0.963	0.028
2,447,453.981	2.734	18.423	0.970	0.027
2,447,454.921	5.093	27.288	0.964	0.027
2,447,454.957	4.934	22.135	0.908	0.026
2,447,454.969	4.878	20.049	0.919	0.026
2,447,454.980	4.833	18.155	0.967	0.026
2,447,454.993	4.778	15.552	0.986	0.027
2,447,455.003	4.741	13.491	0.978	0.027
2,447,455.015	4.705	11.115	0.972	0.027
2,447,455.024	4.680	9.062	0.977	0.026
2,447,455.037	4.653	6.185	0.933	0.032
2,447,455.050	4.636	3.183	0.960	0.027
2,447,455.928	6.587	25.980	0.881	0.030
2,447,455.945	6.490	23.593	0.845	0.030
2,447,455.962	6.384	20.683	0.899	0.030
2,447,455.974	6.319	18.661	0.856	0.029
2,447,455.985	6.258	16.546	0.900	0.030
2,447,455.996	6.204	14.363	0.920	0.030
2,447,456.007	6.155	12.078	0.922	0.031
2,447,456.018	6.114	9.724	0.941	0.031
2,447,456.030	6.079	7.157	0.939	0.031
2,447,456.041	6.055	4.478	0.928	0.030
2,447,438.947	18.608	29.260	0.364	0.013
2,447,438.968	18.309	26.817	0.380	0.012
2,447,438.988	17.984	23.980	0.395	0.012
2,447,439.024	17.413	17.976	0.415	0.013
2,447,439.043	17.146	14.289	0.438	0.014
2,447,456.916	22.193	27.143	0.244	0.006
2,447,456.935	21.836	24.598	0.250	0.006
2,447,457.046	20.215	2.793	0.320	0.016
2,447,457.964	21.220	19.514	0.271	0.006
2,447,457.976	20.984	17.152	0.290	0.007
2,447,457.993	20.703	13.805	0.306	0.006
2,447,458.008	20.505	10.815	0.312	0.006
2,447,458.019	20.377	8.311	0.307	0.007
2,447,458.034	20.256	4.843	0.335	0.007
2,447,458.044	20.213	2.678	0.332	0.007
2,447,458.053	20.195	0.435	0.335	0.007
2,447,460.952	29.068	20.149	0.068	0.003
2,447,460.970	28.613	16.858	0.079	0.004
2,447,478.899	26.960	20.833	0.108	0.007
2,447,478.935	26.154	14.128	0.125	0.009
2,447,478.950	25.887	11.006	0.139	0.010
2,447,478.965	25.679	7.698	0.149	0.010
2,447,484.836	28.099	27.661	0.077	0.016
2,447,484.867	27.366	23.477	0.103	0.010
2,447,484.878	27.077	21.631	0.121	0.015
2,447,484.884	26.926	20.595	0.103	0.011
2,447,484.891	26.773	19.497	0.117	0.014
2,447,484.897	26.630	18.398	0.120	0.017
2,447,484.939	25.806	9.841	0.143	0.013
2,447,484.951	25.659	7.303	0.147	0.015
2,447,484.962	25.552	4.594	0.146	0.014
2,447,484.974	25.493	1.879	0.143	0.012

linear interpolation in $\log \lambda - \log F_\lambda$ space. We have adopted a uniform flux uncertainty of 5% for all the spectrophotometric data. The most carefully calibrated photometric standards are not likely to be more accurate than 4% in the absolute sense (Bohlin & Gilliland 2004). On the basis of Procyon's distance (3.5 pc), interstellar dust extinction is assumed to be negligible. The integrated flux from 170 to 10,200 nm is $(17.82 \pm 0.89) \times 10^{-9}$ W m^{-2}. This value is in good agreement with the value 18.08 ± 0.76 W m^{-2} derived by Code et al. (1976). The difference in the integrated flux between STIS and *IUE* over their common wavelength range is less than 1%. The integrated STIS flux is ∼6% larger than the integrated Glushneva et al. (1992) flux between 322 and 410 nm. Our integrated flux and the limb-darkened angular diameter ($\theta_{\text{LD}} = 5.45 \pm 0.05$ mas) from Kervella et al. (2004b) yield $T_{\text{eff}} = 6516 \pm 87$ K. This value is in good agreement with $T_{\text{eff}} = 6510 \pm 150$ K from Code

TABLE 3—*Continued*

Julian Date	Projected Baseline (m)	Position Angle (deg)	V^2	$\sigma V^2_{\text{total}}$
2,447,484.981........................	25.482	0.339	0.154	0.013
2,447,484.987........................	25.486	−1.146	0.135	0.011
2,447,484.993........................	25.502	−2.497	0.124	0.016
2,447,833.958........................	24.330	14.949	0.184	0.002
2,447,833.974........................	24.055	11.678	0.197	0.003
2,447,833.983........................	23.923	9.706	0.209	0.003
2,447,833.989........................	23.855	8.511	0.202	0.003
2,447,833.997........................	23.767	6.625	0.206	0.003
2,447,834.002........................	23.722	5.442	0.209	0.003
2,447,834.011........................	23.670	3.558	0.217	0.005
2,447,834.024........................	23.632	0.512	0.214	0.004
2,447,834.029........................	23.633	−0.749	0.198	0.004
2,447,834.036........................	23.648	−2.353	0.208	0.003
2,447,834.042........................	23.673	−3.700	0.203	0.004
2,447,834.049........................	23.715	−5.208	0.205	0.003
2,447,834.055........................	23.766	−6.598	0.207	0.006
2,447,834.061........................	23.831	−8.048	0.182	0.007

et al. (1976). A comparison of the angular diameter uncertainty (0.9%) and the integrated flux uncertainty (5%) shows that the uncertainty in T_{eff} is dominated by the uncertainty in the spectrophotometry.

2.2.2. *Radius and Surface Gravity*

The *Hipparcos* parallax (285.93 ± 0.88 mas; Perryman et al. 1997) and the angular diameter ($\theta_{\text{LD}} = 5.45 \pm 0.05$ mas) yield a radius of 2.05 ± 0.02 $R_\odot$. The orbital solution of Girard et al. (2000) provides a mass for Procyon A, which is 1.42 ± 0.04 $M_\odot$ adopting the *Hipparcos* parallax (Kervella et al. 2004b). The mass, together with the radius, yields a surface gravity $\log g = 3.95 \pm 0.02$ (in cgs units), which is uncertain at the 5% level.

3. MODEL ATMOSPHERES

The construction of model atmospheres for Procyon and the subsequent calculation of synthetic radiation fields for comparison with interferometry and photometry is done three ways: (1) stand-alone one-dimensional PHOENIX (Hauschildt et al. 1999) structures, radiation fields, and spectra; (2) CO⁵BOLD (Freytag et al. 2002) three-dimensional structures temporally and spatially averaged to one-dimension, then read by PHOENIX for computation of the corresponding radiation fields; and (3) stand-alone one-dimensional ATLAS 12 (Kurucz 1992) structures, radiation fields, and spectra. These models will be discussed in more detail below.

3.1. *Input Parameters*

The ATLAS 12 models are plane parallel and require an effective temperature T_{eff} and a surface gravity $\log g$ as input parameters. The spherical PHOENIX models additionally require a stellar radius because in the spherical case the luminosity, not the flux, is constant. For Procyon's photosphere this distinction is negligible; however, the boundary radii of the spherical and plane-parallel models differ, as discussed below. CO⁵BOLD models a local, three-dimensional, statistically representative volume of the stellar atmosphere in Cartesian geometry with periodic lateral boundaries. As input parameters, CO⁵BOLD requires the surface gravity and the specific entropy of material entering the computational volume through the open lower boundary. The entropy strongly influences the amount of heat entering the vol-

ume from below and plays a role analogous to the effective temperature in the one-dimensional models.

3.2. *PHOENIX Models*

A grid of 42 one-dimensional, spherical, hydrostatic models from the PHOENIX general-purpose stellar and planetary atmosphere code (ver. 13.07; for a description see Hauschildt et al. 1999; Hauschildt & Baron 1999) have been constructed with the following parameters: effective temperatures $T_{\text{eff}} = 6420$–6620 K, 10 K steps; $\log g = 3.95$; radius $R = 1.46 \times 10^{11}$ cm; depth-independent microturbulence $\xi = 2.0$ km s^{-1} (a value suggested for one-dimensional models by AP02 from their analysis of Procyon's spectrum); mixing length to pressure scale ratio $\alpha = 0.5$ and 1.25; solar elemental abundance (Anders & Grevesse 1989); LTE atomic and molecular line blanketing, typically 10^6 atomic lines and 4×10^5 molecular lines dynamically selected at run time; non-LTE line blanketing of H I (30 levels, 435 bound-bound transitions), He I (19 levels, 171 bound-bound transitions), and He II (10 levels, 45 bound-bound transitions); and the boundary conditions, including outer pressure, $P_{\text{gas}} = 10^{-4}$ dynes cm^{-2}, and extinction optical depth at 1.2 μm, outer = 10^{-10} and inner = 10^2. For this grid of models the atmospheric structure is computed at 100 radial shells (depths) and the radiative transfer is computed along 100 rays tangent to these shells and 14 additional rays that impact the innermost shell, the so-called core-intersecting rays. The intersection of the rays with the outermost radial shell describes a center-to-limb intensity profile with 114 angular points. The mixing-length theory for convection in PHOENIX is very similar to the Mihalas formulation (Ludwig et al. 2002; Mihalas 1978) with no overshooting. A second grid of 24 PHOENIX models has been constructed as components of composite models that simulate the effects of granulation on the SED (see § 3.6, Table 4). Other than T_{eff}, these models have the same input parameters as the first grid. The non-LTE H and He aspect of the stand-alone PHOENIX models is an insignificant factor for the angular diameter fits and synthetic spectrophotometry presented here, as we have confirmed by converging purely LTE PHOENIX models for comparison. The H$^-$ ion is treated in LTE for all the PHOENIX models. The effects of treating many thousands of lines out of LTE in a solar-type star has been recently explored by Short & Hauschildt (2005). Such effects could be important for the synthetic spectrophotometry; however, such massive-scale non-LTE models for Procyon have yet to be calculated and are beyond the scope of this paper. Below we specifically refer to PHOENIX models "A" and "B." For both models, $T_{\text{eff}} = 6530$ K and $\log g = 3.95$ (consistent with the values derived in § 2.2), but the models have different values for α, 1.25 and 0.5, respectively.

3.3. *CO⁵BOLD and PHOENIX Models*

The "COnservative COde for COmputation of COmpressible COnvection in a BOx of L Dimensions ($L = 2,$ 3)" (CO⁵BOLD) was mainly developed by B. Freytag and M. Steffen (for details see Freytag et al. 2002; Wedemeyer et al. 2004). The CO⁵BOLD models (series codes d3gt65g40n2.80-a4-3 [gray] and d3gt65g40n3.10-26-3 [nongray]) for Procyon have an average $T_{\text{eff}} = 6500$ K, a prescribed $\log g = 4.0$, and solar abundances. For the nongray model, five wavelength groups are employed to describe the wavelength dependence of the radiation field within a multigroup radiative transfer scheme (Ludwig 1992). The group-averaged opacities are based on data provided by the ATLAS 6 code (Kurucz 1979).

Integration with the one-dimensional PHOENIX code provides direct opacity sampling at high spectral resolution for

TABLE 4
Synthetic Strömgren Indices for Composite SED Components

Surface Area Weight	T_{eff} (K)	$\log g$	α	$b - y$	c_1
Composite SED A, $\beta = 0.6$ Linear Limb Darkening					
0.002............................	5483	3.95	1.25	0.452	0.469
0.027............................	5693	3.95	1.25	0.416	0.446
0.093............................	5893	3.95	1.25	0.384	0.436
0.125............................	6074	3.95	1.25	0.356	0.445
0.120............................	6241	3.95	1.25	0.332	0.464
0.108............................	6395	3.95	1.25	0.311	0.491
0.114............................	6538	3.95	1.25	0.291	0.521
0.134............................	6672	3.95	1.25	0.274	0.554
0.139............................	6799	3.95	1.25	0.257	0.586
0.106............................	6920	3.95	1.25	0.242	0.620
0.029............................	7034	3.95	1.25	0.227	0.652
0.002............................	7145	3.95	1.25	0.213	0.684
Composite SED B, $\beta = 0.5$ Linear Limb Darkening					
0.002............................	5539	3.95	1.25	0.442	0.461
0.027............................	5751	3.95	1.25	0.406	0.444
0.093............................	5953	3.95	1.25	0.375	0.437
0.125............................	6136	3.95	1.25	0.347	0.451
0.120............................	6304	3.95	1.25	0.323	0.474
0.108............................	6460	3.95	1.25	0.302	0.504
0.114............................	6604	3.95	1.25	0.283	0.536
0.134............................	6740	3.95	1.25	0.265	0.571
0.139............................	6869	3.95	1.25	0.248	0.606
0.106............................	6990	3.95	1.25	0.233	0.639
0.029............................	7106	3.95	1.25	0.218	0.672
0.002............................	7217	3.95	1.25	0.205	0.704

calculation of the radiation field based on temperature structures provided by CO⁵BOLD. The one-dimensional temperature, pressure, and depth arrays (91 depth points) from CO⁵BOLD are read by PHOENIX. The physical depths provided by CO⁵BOLD are relative to the layer where the average Rosseland optical depth is unity, but PHOENIX requires absolute radii for construction of the one-dimensional spherical radiation field. The value 1.46×10^{11} cm, corresponding to the physical radius of Procyon, is therefore added to the CO⁵BOLD depths. The accuracy of this value is not critical because the thickness of the atmosphere is ~0.1% of the stellar radius.

We take two approaches for the computation of the mean radiation field of the CO⁵BOLD models. (1) We compute a PHOENIX radiation field from a temporally and spatially averaged three-dimensional temperature structure. (2) We compute 980,000 horizontal positions from the spatial and temporal evolution of the granular flow (see Fig. 1 for a snapshot of the flow) and sort them into 12 groups according to their intensity (see Fig. 2 for the histogram of intensities). Next, we average the vertical slabs on surfaces of fixed optical depth. This results in 12 temperature stratifications representing the dark and increasingly brighter granulation areas. PHOENIX radiation fields are then computed for each of the 12 structures. These radiation fields are then co-added and weighted by the surface areas of the 12 intensity groups (for weights see Table 4). Theoretically, we expect that approach 2 provides a better match to the actual radiation field of Procyon. This is because radiative transfer in an inhomogeneous medium is nonlinear and one cannot interchange radiative transfer and spatial averaging exactly. In this respect, the 12 component model should be an improvement over a global spatial mean.
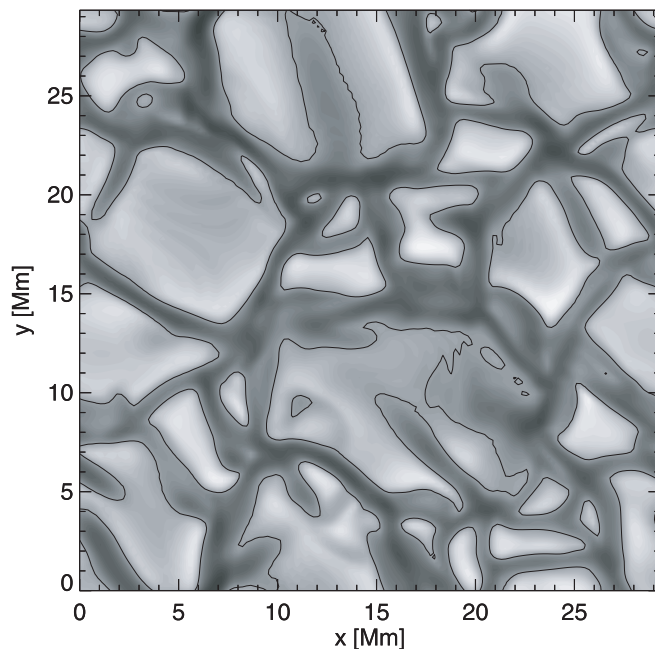

Fig. 1.—Typical map of the emergent white light intensity in the vertical direction encountered during the temporal evolution of the gray CO⁵BOLD model. The black line depicts an isophote at 3.95×10^{10} ergs cm^{-2} sr^{-1} s^{-1} approximately corresponding to the image's median intensity (see Fig. 2).

We find that the temporally and spatially averaged temperature structures from the gray and nongray CO⁵BOLD models are nearly identical at the depths of continuum formation for the interferometric wavebands considered here: 500 nm, 800 nm, and 2.2 μm. As a result, the corresponding PHOENIX radiation fields from approach 1 yield fit angular diameters that differ by less than 0.03%. Much greater than the gray versus nongray effects are the differences using approaches 1 and 2. Using the weighted average of the 12 radiation fields to simulate the mean center-to-limb profile yields an angular diameter 0.4% larger at 500 nm compared to the global spatial mean radiation field. As we show in § 4, approach 2 is slightly more consistent with the observed visibility data. Below we refer to models "C1" and "C2," models constructed via approaches 1 and 2, respectively.

Tests indicate that the PHOENIX radiation field produced from the CO⁵BOLD one-dimensional average structure produces
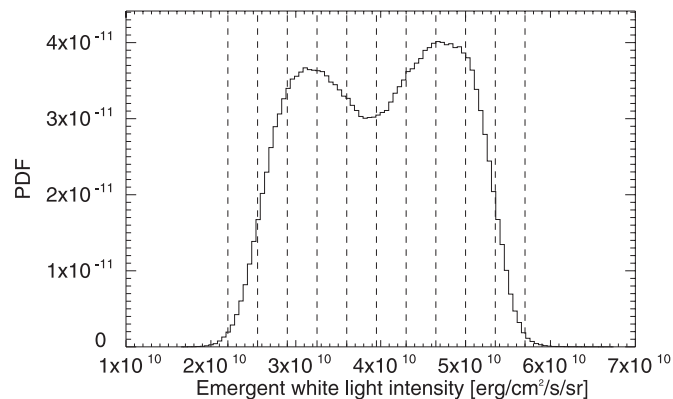

Fig. 2.—Probability density function (PDF), the probability per differential intensity interval with the units of inverse intensity, of the emergent white light intensity of the gray CO⁵BOLD model. The PDF was derived from a sequence of intensity maps like the one shown in Fig. 1. Twelve intensity intervals are demarcated by the dashed lines. The surface area weights for these intervals are given in Table 4.

an outer boundary radiative flux lower than expected (by 15% in flux, 260 K in T_{eff}) for an effective temperature of 6500 K. This is most likely due to the different opacity setups in the two codes. $\mathrm{CO^5BOLD}$ uses the older ATLAS 6 opacity setup. As a result, a SED from PHOENIX based on the mean three-dimensional structure will be cooler than expected from the $\mathrm{CO^5BOLD}$ T_{eff} value. This is not a critical problem for the interferometric comparisons because of the insensitivity of the LD to T_{eff} in this range (5500–7500 K; see § 5.2). The radiative flux mismatch is a problem with regards to synthetic photometry, and this is discussed below in § 3.6.

3.4. *ATLAS 12 Models*

We also use ATLAS 12 models (Kurucz 1992; R. L. Kurucz 2004, private communication), which include an "approximate overshooting" prescription for convective flux transport in a mixing-length formalism (Castelli et al. 1997, § 2.3), for comparison with the one-dimensional and three-dimensional models just discussed. In the approximate-overshooting formulation, the convective flux extends to lower optical depths, reducing the temperature gradient relative to models without overshooting. Three ATLAS 12 models have been constructed: D, no overshooting; F, 50% overshooting; and E, full overshooting. All three models have the following parameters: $T_{\mathrm{eff}} = 6530$ K; $\log g = 3.95$; the microturbulence is depth dependent, increasing from 0.9 to 3.2 km s^{-1} at the inner boundary; $\alpha = 1.25$; solar elemental abundance (Anders & Grevesse 1989); LTE atomic and molecular line blanketing; and the boundary conditions outer $\tau_{\mathrm{Ross}} = 10^{-7}$ and inner $\tau_{\mathrm{Ross}} = 10^2$. After the models, with 72 depth points, were computed by opacity sampling, the complete spectrum was computed at a resolving power of $R = 500{,}000$ for 17 angular "μ-points" describing the center-to-limb intensity profile.

3.5. *Synthetic Visibilities and Fit Procedure*

The computation of the synthetic visibilities from the model radiation fields simulates the bandwidth-smeared squared visibility (see, e.g., Davis et al. 2000). At a projected baseline B and mean wavenumber λ_0^{-1}, the synthetic squared visibility,

$$V(B, \lambda_0)^2 = \frac{\int_0^\infty V(B, \lambda)^2 \lambda^2 \, d\lambda}{\int_0^\infty S(\lambda)^2 F_\lambda^2 \lambda^2 \, d\lambda}, \qquad (2)$$

is computed at each wavelength from a Hankel transform,

$$V(B, \lambda) = \int_0^1 S(\lambda) I(\mu, \lambda) J_0 \left[\pi \theta_{\mathrm{LD}} (B/\lambda)(1 - \mu^2)^{1/2} \right] \mu \, d\mu, \quad (3)$$

where $I(\mu, \lambda)$ is the model radiation field (in photons cm^{-2} s^{-1} sr^{-1}), $S(\lambda)$ is the instrument sensitivity curve, μ is the cosine of the angle between the line of sight and the surface normal, and θ_{LD} is the limb-darkened angular size. The mean wavenumber is computed from

$$\lambda_0^{-1} = \frac{\int_0^\infty \lambda^{-1} S(\lambda) F_\lambda \, d\lambda}{\int_0^\infty S(\lambda) F_\lambda \, d\lambda}, \qquad (4)$$

where

$$F_\lambda = 2\pi \int_0^1 I(\mu, \lambda) \mu \, d\mu \qquad (5)$$

is the flux. For each model radiation field, nonlinear least-squares fits are performed to the visibility data at 500 nm, 800 nm, and 2.2 μm, using the Interactive Data Language (IDL) routine `curvefit`, yielding three values for θ_{LD}.

The baselines for the VINCI visibilities are listed in Table 1. The reciprocal of the mean wavenumber for the VINCI transmission (including K-band filter, detector quantum efficiency, fibers, atmosphere, and MONA beam combiner) is $\lambda_0 = 2.182 \pm 0.002$ μm using an appropriate synthetic spectrum for Procyon (a $T_{\mathrm{eff}} = 6530$ K, $\log g = 3.95$ PHOENIX model). An accurate estimate for the mean wavenumber is important because the fit angular diameter scales linearly with the mean wavenumber.

The Mark III sensitivity curves are assumed to be Gaussian with central wavelengths $\lambda_0 = 500$ and 800 nm, each with a FWHM of 20 nm (Mozurkewich et al. 1991). The Mark III bands are ∼20 times narrower than the VINCI band; therefore the mean wavenumber is much less sensitive to the shape of Procyon's SED.

3.5.1. *Accounting for Extension in the Spherical Models*

A proper comparison of the best-fit θ_{LD} values derived from the PHOENIX, $\mathrm{CO^5BOLD}$+PHOENIX, and ATLAS 12 models requires a correction to the stand-alone PHOENIX values because of spherical extension effects. The PHOENIX structures extend outward to a radial shell $\simeq 0.4\%$ above the $\tau_{\mathrm{Ross}} = 1$ radius, while the model plane-parallel structures have very small extensions for a fixed gravity (the $\mathrm{CO^5BOLD}$ and ATLAS 12 structures have extensions of $\simeq 0.1\%$). The radiation field $I(\mu, \lambda)$ refers to the angular distribution of intensities emerging from the outermost model layer. As a result, the spherical models with greater radial extension yield larger angular sizes relative to the less extended plane-parallel models. This is true even when the angular sizes of the continuum-forming radii for the two model geometries agree, because their outer boundary radii differ. Thus, the PHOENIX θ_{LD} values have been scaled down to correspond with the $\tau_{\mathrm{Ross}} = 1$ radius (in other words, reduced by 0.4%) for comparison with the plane-parallel models. For red giants the correction is much larger, for example 7% in the case of ψ Phe (Wittkowski et al. 2004). This correction reminds us that even relatively compact atmospheres are "fuzzy" and that the stellar radius must be carefully defined (Baschek et al. 1991). The need for this correction also speaks to the precision of the observational data.

3.6. *Synthetic Spectrophotometry and Photometry with Three-dimensional and One-dimensional Models*

At present, the coarseness of the wavelength-dependent opacity in the $\mathrm{CO^5BOLD}$ model does not permit direct predictions of accurate colors. Therefore, we use the spatial intensity distribution of the three-dimensional model as a guide to construct multicomponent models of Procyon's granulation pattern with PHOENIX. From the gray $\mathrm{CO^5BOLD}$ model a snapshot of the emergent intensity in integrated ("white") light is shown in Figure 1; Figure 2 depicts a histogram of intensities, including 12 intensity intervals for which we construct PHOENIX models (see Table 4 for corresponding surface area weights). The bimodal nature of the histogram shows that the model photosphere can be divided roughly into "cool" and "hot" components, as also indicated in the intensity map. In fact, we initially experimented with such a two-component model, and later refined the spectral synthesis to the present 12 component model.

TABLE 5
Fit Angular Diameters

Model	Parameters	Mark III, 500 nm (mas)	Mark III, 800 nm (mas)	VLTI VINCI, 2.2 μm (mas)
PHOENIX:				
A..........................	$T_{\rm eff}$ = 6530 K, log g = 3.95, α = 1.25	5.449 ± 0.012	5.416 ± 0.005	5.411 ± 0.006
B..........................	$T_{\rm eff}$ = 6530 K, log g = 3.95, α = 0.5	5.468 ± 0.012	5.415 ± 0.005	5.410 ± 0.006
CO^{5}BOLD+PHOENIX:				
C1........................	$T_{\rm eff}$ = 6500 K, log g = 4.0, global mean structure	5.387 ± 0.011	5.388 ± 0.005	5.402 ± 0.006
C2........................	$T_{\rm eff}$ = 6500 K, log g = 4.0, 12 weighted structures	5.409 ± 0.011	5.393 ± 0.005	5.405 ± 0.006
ATLAS 12:				
D.........................	$T_{\rm eff}$ = 6530 K, log g = 3.95, α = 1.25, no overshooting	5.426 ± 0.011	5.404 ± 0.005	5.404 ± 0.006
E	$T_{\rm eff}$ = 6530 K, log g = 3.95, α = 1.25, 100% overshooting	5.368 ± 0.011	5.383 ± 0.005	5.394 ± 0.006
F	$T_{\rm eff}$ = 6530 K, log g = 3.95, α = 1.25, 50% overshooting	5.400 ± 0.011	5.398 ± 0.005	5.402 ± 0.006
Uniform disk, U....................	$V^2 = \left| 2J_1(\pi\theta_{\rm UD}B/\bar{\lambda})/(\pi\theta_{\rm UD}B/\bar{\lambda}) \right|^2$	5.044 ± 0.010	5.208 ± 0.005	5.302 ± 0.005

For constructing the PHOENIX models we need to specify a $T_{\rm eff}$. Assuming a linear darkening law

$$\frac{I_\lambda(\mu)}{I_\lambda(1)} = 1 - \beta(1-\mu), \qquad (6)$$

we convert emergent intensities in the vertical direction to fluxes F according to

$$F_\lambda = \pi I_\lambda(1)\left(1 - \frac{\beta}{3}\right). \qquad (7)$$

With the additional assumption of a wavelength-independent β, we directly obtain $T_{\rm eff}$ since the gray CO^{5}BOLD model provides wavelength-integrated intensities. The $T_{\rm eff}$ of the inner 10 zones are taken as the average of the $T_{\rm eff}$ at the two adjacent boundaries. For the two outer zones, half the interval width $\Delta T_{\rm eff}$ of the adjacent zone is added (subtracted) to the hottest (coolest) boundary. The radiation fields of the individual components are added, weighted by the surface area fraction associated with the represented intensity interval. The resulting $T_{\rm eff}$ values and weights for the 12 zones are listed in Table 4. Two values for β have been chosen: 0.5 and 0.6. These values are consistent with published linear LD coefficients for broadband optical filters (Claret 2000). More importantly, these two β-values yield $T_{\rm eff}$ distributions that, after the 12 one-dimensional model SEDs are weighted and co-added, have bolometric fluxes and corresponding effective temperatures that bracket the CO^{5}BOLD model ($T_{\rm eff}$ = 6500 K). The composite spectrum $T_{\rm eff}$ is computed as

$$T_{\rm eff} = \left[\frac{1}{\sigma}\int_0^\infty \left(\sum_{i=1}^{i=12} w^i F_\lambda^i\right) d\lambda\right]^{1/4}, \qquad (8)$$

where σ is the Stefan-Boltzmann constant, w^i are the weights given in Table 4, and F_λ^i are the flux distributions from the component models.

3.6.1. Synthetic Photometry

Synthetic Strömgren indices (Strömgren 1966) are computed using the formulae of Matsushima (1969). In this formalism, a normalization constant, or zero point, k_{ij} is needed to transform each natural index

$$(i-j)_{\rm nat} = 2.5 \log\left[\frac{\int_0^\infty F_\lambda S_j(\lambda)\, d\lambda}{\int_0^\infty F_\lambda S_i(\lambda)\, d\lambda}\right] \qquad (9)$$

to a photometric index

$$i - j = (i - j)_{\rm nat} + k_{ij} \qquad (10)$$

directly comparable to observations. In the literature, the normalization of the theoretical indices is often based solely on models of Vega (e.g., Smalley & Kupka 1997); however, Lester et al. (1986) have shown that these zero points are a function of $b - y$. Since Vega and Procyon do not have the same $b - y$, using Vega leads to systematic errors in the synthetic indices. We also wish for obvious reasons not to use a model of Procyon to obtain these zero points. Therefore, we use two independent spectrophotometric observations of Procyon (Kiehling 1987; Glushneva et al. 1992) and two different sets of filter sensitivity curves (Matsushima 1969; Crawford & Barnes 1970) to determine the following zero points:

$$(b - y)_{\rm obs} - (b - y)_{\rm nat} = +0.503 \pm 0.004 \pm 0.007, \qquad (11)$$
$$(c_1)_{\rm obs} - (c_1)_{\rm nat} = -0.088 \pm 0.003 \pm 0.009. \qquad (12)$$

These zero points are given with two sets of uncertainties. The first set arises from the range of zero points obtained using the four different filter/spectrophotometric data combinations. The second set is from to the mean observational error in the observed indices (Crawford & Barnes 1970). If we use spectrophotometry of Vega (Bohlin 1996), the mean c_1 zero point is instead -0.165 mag, consistent with the c_1 shift shown by Lester et al. (1986) at the $b - y$ color (0.272) of Procyon.

4. RESULTS

4.1. Multiwavelength Angular Diameter Fits

Table 5 lists the best-fit $\theta_{\rm LD}$ values (and 1 σ uncertainties) at 500 nm, 800 nm, and 2.2 μm for seven different atmospheric structures and a uniform-disk model. Figure 3 shows all the visibility data, together with the synthetic visibilities from the CO^{5}BOLD+PHOENIX model C2 with a mean-fit angular diameter of 5.403 mas. The best-fit angular diameters for all seven models are compared in Figure 4.

There is a clear trend in the fit results toward shorter wavelengths. The seven models yield a significantly wide range of angular diameters at 500 nm, differing by 100 ± 23 μas, while differing only by 17 ± 12 μas at 2.2 μm. Of the seven models, two models stand out as best representing the visibility data at all three wavelengths with a single angular diameter:

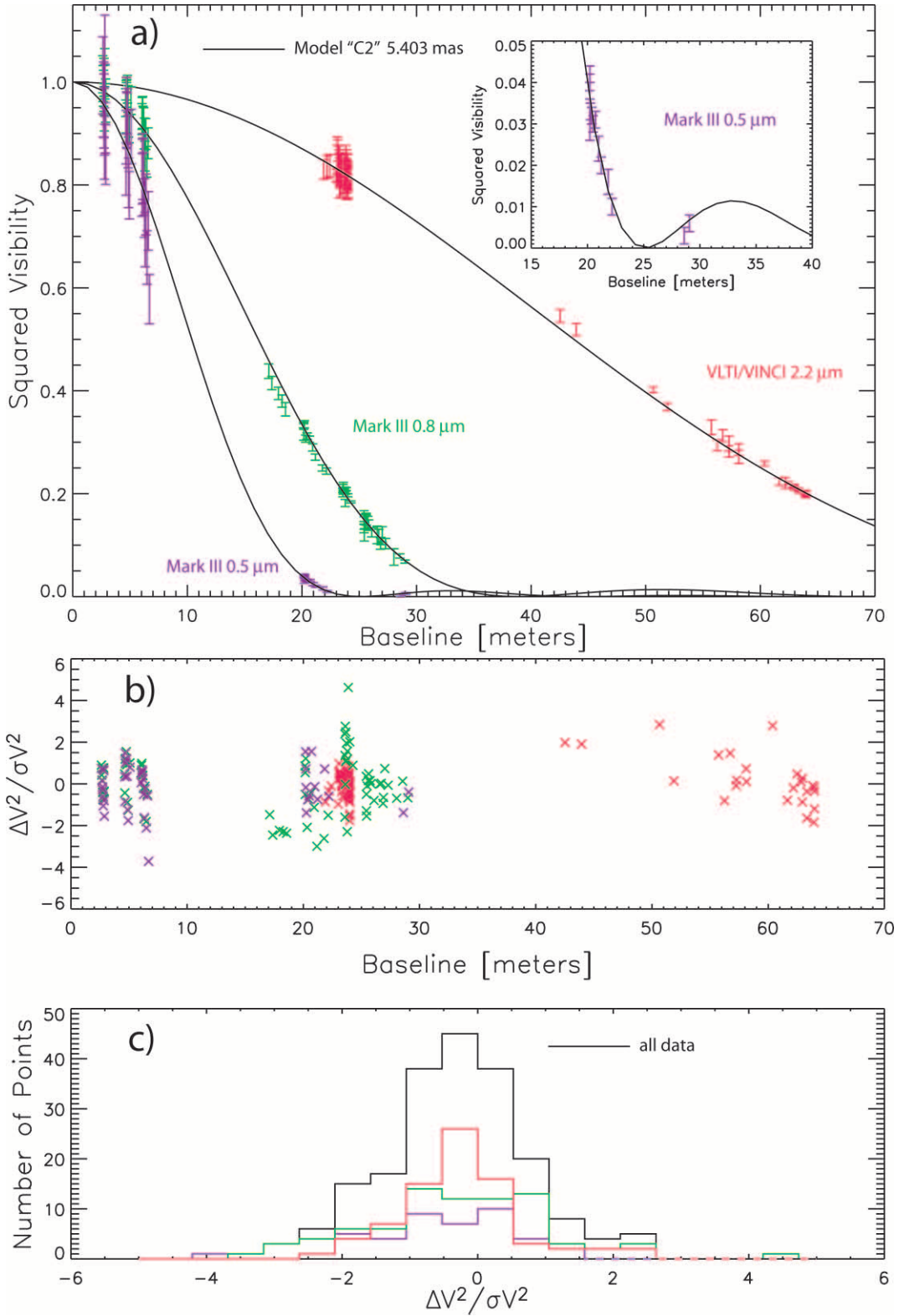FIG. 3.—(*a*) Squared visibility data from Tables 1 (*red*), 2 (*purple*), and 3 (*green*) as a function of projected baseline compared to the synthetic visibilities (from eq. [2]) from the three-dimensional CO⁵BOLD+PHOENIX model C2 with an angular diameter of 5.403 mas. (*b*) Deviations of each data set from the model. (*c*) Histograms of these deviations for each data set and for all the data combined.
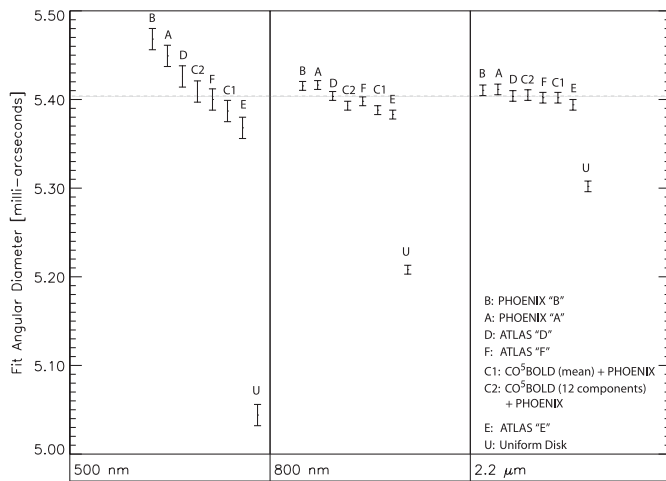
Fig. 4.—Comparison of the best-fit angular diameters θ_{LD} at 500 and 800 nm (Mark III data) and 2.2 μm (VLTI data) from Table 5 for the seven atmosphere models A–F and U (uniform-disk model). The uniform-disk angular diameters indicate that Procyon is more limb darkened at shorter wavelengths, as expected. The atmosphere model fits are more dispersed at shorter wavelengths. The fits indicate that one-dimensional models without overshooting are too limb darkened at 500 nm, while one-dimensional model E with 100% overshooting is not limb darkened enough. Model F with 50% overshooting yields the same angular diameter (within 1 σ) at all three wavelengths. The three-dimensional CO^{5}BOLD+PHOENIX models C1 and C2 yield angular diameters slightly less consistent than model F, but with no free parameters for convection. The dashed line indicates the angular diameter of the model in Fig. 3.

CO^{5}BOLD+PHOENIX model C2 and ATLAS 12 model F (with 50% overshooting). Both models yield angular diameters at 500 nm and 2.2 μm that are the same within the formal uncertainties: 15 ± 17 and 4 ± 17 μas, respectively. Unlike model F, model C2 has no free parameters for convection.

4.2. Model Comparisons to Spectrophotometry and Photometry

Figure 5a shows that the synthetic SED of ATLAS 12 model E fails to reproduce the observed continuum below 160 nm. This is true not only for model E but for all one-dimensional models, regardless of convection treatment, that are consistent with both the measured angular diameter and the measured bolometric flux. While the contribution to Procyon's bolometric flux from radiation between 130 and 160 nm is negligible, the absolute flux level in this region provides strong evidence for a multicomponent temperature surface distribution and therefore granulation.

The absolute continuum fluxes between 136 and 160 nm are from the Goddard High Resolution Spectrograph data sets: Z2VS0105P (PI A. Boesgaard) and Z17X020CT, Z17X020AT, and Z17X0208T (PI J. Linsky). These spectra were originally obtained to study Procyon's atmospheric boron abundance (Cunha et al. 2000) and chromosphere (Wood et al. 1996). The signal-to-noise ratio in the continua of these spectra ranges from approximately 4 : 1 in the bluest data set to 10 : 1 in the reddest data set. These data are far superior to any other measurements below 160 nm because the continuum drops by more than a factor of 100 here, too much for the limited dynamic range of *IUE*. The
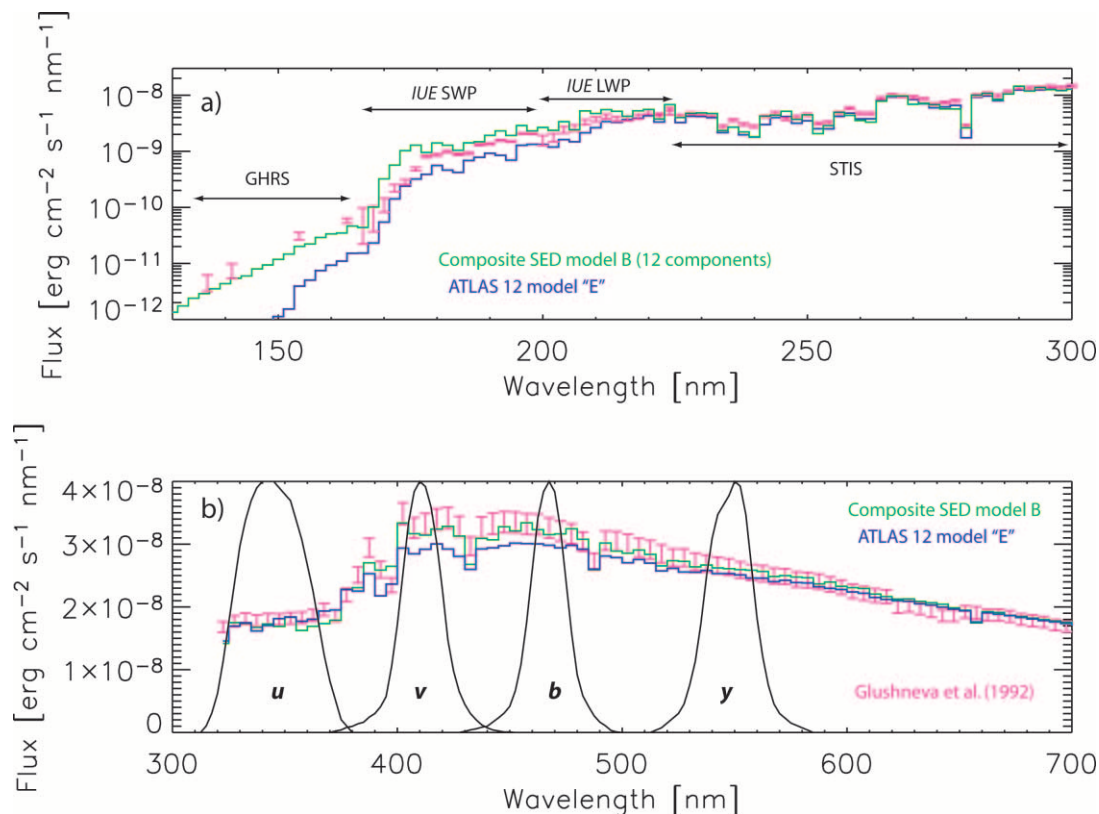
Fig. 5.—Comparisons between synthetic SEDs and spectrophotometric measurements at ultraviolet and visual wavelengths. The models and data are binned to 2 nm resolution in the UV for clarity. The models are binned to 5 nm in the visual to match the resolution of the spectrophotometry. The synthetic SEDs are scaled in absolute flux using an angular diameter of 5.40 mas, a value consistent with our best interferometric estimate (see Table 7). (*a*) Composite SED model B (*green*), which incorporates a three-dimensional model for the distribution of surface intensities due to granulation and better represents the UV flux distribution than a single T_{eff} component one-dimensional model (*blue*; ATLAS 12 model E), particularly at wavelengths below 160 nm, where all five single T_{eff} component one-dimensional atmosphere models fail. (*b*) Composite SED model B (*green*) yields Strömgren *v*- and *b*-band fluxes consistent with the observed spectrophotometry (Glushneva et al. 1992) and larger than the single T_{eff} component model (*blue*; ATLAS 12 model E). These two models are in closer agreement in the *u* and *y* bands.

TABLE 6
SYNTHETIC STRÖMGREN INDICES

Model	$T_{\rm eff}$ (K)	log g	Additional Parameters	$b - y$[a]	c_1[a]
ATLAS 12:					
E........................	6530	3.95	$\alpha = 1.25$, overshooting	0.321	0.378
F	6530	3.95	$\alpha = 1.25$, 50% overshooting	0.311	0.402
D........................	6530	3.95	$\alpha = 1.25$, no overshooting	0.302	0.437
PHOENIX:					
A........................	6530	3.95	$\alpha = 1.25$	0.292	0.519
B........................	6530	3.95	$\alpha = 0.50$	0.282	0.547
Composite SED:					
A........................	6466	3.95	$\beta = 0.60$ linear limb darkening	0.293	0.539
B........................	6531	3.95	$\beta = 0.50$ linear limb darkening	0.283	0.553

[a] Interstellar reddening toward Procyon is assumed to be negligible: $b - y = (b - y)_0$, $c_1 = c_0$. Observed values: $b - y = 0.272$ (Crawford & Barnes 1970; Nordström et al. 2004) and $c_1 = 0.532$ (Crawford & Barnes 1970).

absolute fluxes below 160 nm shown in Figure 5 were estimated by computing the mean flux between the emission lines in each spectrum incorporating the flux uncertainties provided with each calibrated data set.

The observed continuum below 160 nm is consistent with a spatial component of Procyon's atmosphere, which has a color temperature in excess of the interferometric $T_{\rm eff}$. Therefore, such a component must represent a small fraction of the surface, for it would otherwise produce a bolometric flux in excess of that observed. The continuum of Procyon between 136 and 160 nm should be photospheric, in contrast to the solar spectrum where the bound-free opacity of silicon causes the continuum to form at or slightly above the temperature minimum, near the base of the chromosphere (Vernazza et al. 1976). Procyon's overall warmer photosphere ($T_{\rm eff} = 6540$ vs. 5770 K) will contribute more flux to this spectral region than does the Sun. Furthermore, the warmer components of Procyon's photosphere, which predominately contribute to the continuum below 160 nm, have a silicon bound-free opacity approximately 3 times weaker than expected for solar photospheric conditions (Travis & Matsushima 1968, Fig. 6). Thus we expect Procyon's continuum between 136 and 160 nm to form at depths beneath its chromosphere.

The ultraviolet SED longward of 160 nm, where the multi-component temperature effects are less prominent, may be impacted by non-LTE treatment of iron-group elements. Short & Hauschildt (2005) find that non-LTE models for the Sun have

substantially (up to 20%) more near-UV flux relative to LTE models. Whether such differences would exist for a similar non-LTE model of Procyon is not clear.

Figure 5b shows that the ATLAS 12 model E SED matches the composite SED B model fairly well in the u and y bands but has significantly lower flux in the b and v bands. In the composite SED model the peaks of the 12 components all contribute flux to the v and b bands, while at longer wavelengths the flux contrast is lower. Table 6 and Figure 6 show that the $T_{\rm eff} = 6530$ K ATLAS 12 models all predict $b - y$ values significantly redder than observed. In particular, the $b - y$ value for ATLAS 12 model F, the best-fitting one-dimensional model to the interferometric data, differs by +0.04 mag, significantly in excess of the estimated uncertainties (0.012 mag; see § 3.6.1).

The differences in the derived indices between PHOENIX model A and ATLAS 12 model D, particularly for c_1, result from differences in these models' temperature structures (see Fig. 7). While these two one-dimensional models were constructed to have the same input parameters, they differ in geometry (spherical vs. plane parallel) and line formation (non-LTE vs. LTE treatment of hydrogen and helium and constant vs. depth-dependent microturbulence) assumptions. To investigate this discrepancy, we converged two LTE, plane-parallel PHOENIX models with constant microturbulences of 0 and 2 km s^{-1}. These models yield colors nearly identical to model A, suggesting that the one-dimensional mixing-length convection treatments (without overshooting) differ between PHOENIX and ATLAS 12. A difference in the convection treatments of these two codes is noted by Short & Hauschildt (2005).

5. DISCUSSION

5.1. Model Differences, Interferometric Uncertainties, and Future Measurements

As predicted by AP02, we find, based on comparisons with high-precision multiwavelength interferometric data, that one-dimensional model temperature structures based on standard mixing-length theory (without overshooting) produce center-to-limb intensity profiles that are too limb darkened at blue wavelengths relative to near-IR wavelengths. The magnitude of this effect appears to be slightly smaller than predicted, 0.4%–1.5% versus 1.6%, depending on which one-dimensional model is adopted. Furthermore, LD predictions from a three-dimensional hydrodynamic model appear to be consistent with these data, also in line with AP02's predictions.
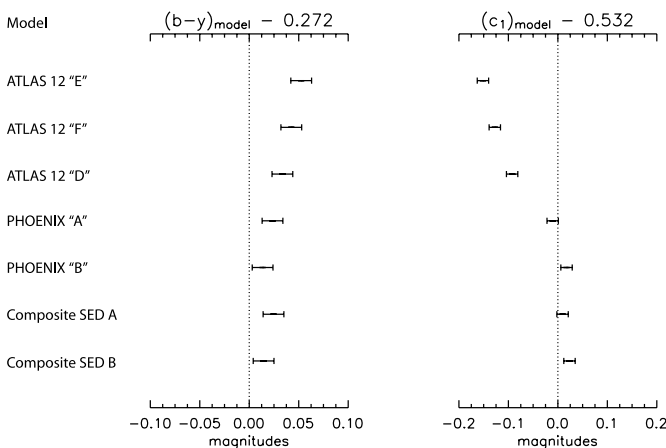

FIG. 6.—Comparison of the synthetic $b - y$ and c_1 Strömgren indices from Table 6 relative to the observed indices (Crawford & Barnes 1970).
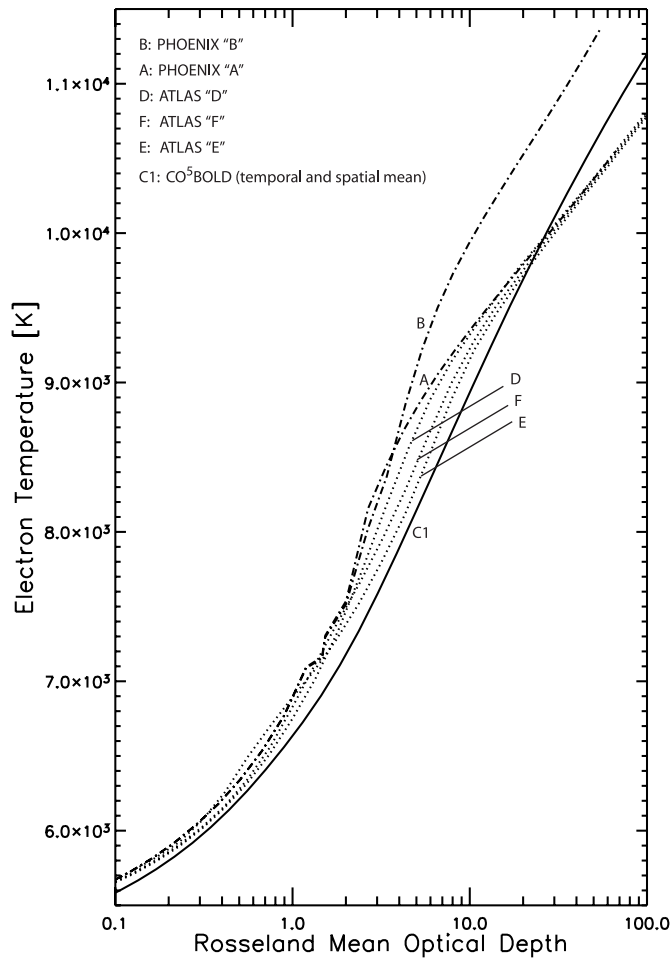
FIG. 7.—Comparison of six model atmosphere temperatures on a mean Rosseland optical depth scale: PHOENIX models A and B (*dash-dotted line*), ATLAS 12 models D, E, and F (*dotted line*), and CO^{5}BOLD model C1 (*solid line*). The degree of LD, particularly at 500 nm where the opacity is relatively low compared to 800 nm and where the intensity contrast as a function of temperature is relatively high compared to 2.2 μm, is sensitive to different convection treatments, which affect the temperature gradient in the interval $\tau_{\rm Ross} = 1$ to $\sim$3. The model with the steepest gradient, PHOENIX B with $\alpha = 0.5$ and no overshooting, has the strongest LD. ATLAS 12 model E with 100% overshooting has the shallowest gradient and the weakest LD. ATLAS 12 model F and CO^{5}BOLD model C1 have similar gradients and provide an intermediate degree of LD, which is consistent with the interferometric observations.

Considering the three ATLAS 12 models, the fit angular diameters differ negligibly (0.2%) at 2.2 μm, but differ by 1.1% at 500 nm due to different convection treatments. Considering all seven model atmospheres, from PHOENIX, ATLAS 12, and CO^{5}BOLD+PHOENIX, the range of fit angular diameters is again small (0.3%) at 2.2 μm, with differences up to 1.9% at

500 nm. The error bars on the interferometric data sets yield formal uncertainties of 0.1% to 0.2% in the absolute angular diameters. It should therefore be possible to choose between these models in the absence of significant systematic errors. Any systematic errors in the VLTI VINCI angular diameters are expected to be less than 0.3% (Kervella et al. 2004b). The systematic errors in the Mark III are not as well characterized; however, the three one-dimensional models without overshooting yield larger angular diameters at 500 nm relative to 800 nm as expected, while the three-dimensional CO^{5}BOLD+PHOENIX model C2 and ATLAS 12 model F for 50% overshooting yield the same angular diameters. These relationships hold out to 2.2 μm, where model C2 yields the same angular diameter within 1.3 σ. This suggests that systematic errors between the VLTI VINCI and Mark III data sets are minimal.

Table 5 and Figure 4 show that an angular diameter derived from the VLTI VINCI visibilities is the least sensitive to which model is employed. The mean angular diameter value at 2.2 μm, together with the 1 σ range in angular diameters (0.26%) and the upper limit on the systematic error in the VLTI VINCI diameter (0.3%), yields a best estimate for the angular diameter of Procyon: 5.404 $\pm$ 0.031 mas. The corresponding best estimates for $T_{\rm eff}$, radius, and surface gravity are listed in Table 7.

Interferometric observations with superior calibration are certainly warranted to check these results. Independent multiwavelength angular diameter measurements are in order; however, this is not the only approach presently available. LD, in addition to its affect on these angular diameter measurements, can be constrained by a precise measurement of the second lobe of the visibility curve. While angular diameters derived from the three-dimensional and standard one-dimensional models differ by only 1% at 500 nm, the squared visibility at the peak of the second lobe is predicted to differ by 10% at 500 nm. At longer wavelengths the predicted difference is smaller: 6% at 800 nm and 3% at 2.2 μm. Precise second-lobe measurements at 500 and 800 nm could possibly be made with the Navy Prototype Optical Interferometer (NPOI) and the Sydney University Stellar Interferometer (SUSI). Distinguishing between the three-dimensional CO^{5}BOLD model and one-dimensional overshooting ATLAS 12 model F on the basis of second-lobe measurements would appear to be much more challenging. The squared visibility amplitudes at the peak of the second lobe for these two models differ by less than 1% at 500 nm, 800 nm, and 2.2 μm.

5.2. *Procyon's Mean Temperature Gradient*

The continuum-forming region of Procyon's atmosphere is expected to have a physical thickness that is very small ($<$0.1%) in comparison with its stellar radius. Therefore, the wavelength-dependent uniform-disk angular diameter is unlikely to result from an extended atmosphere where significantly different physical depths are probed at different wavelengths, as in the case of

TABLE 7
Fundamental Parameters for Procyon A

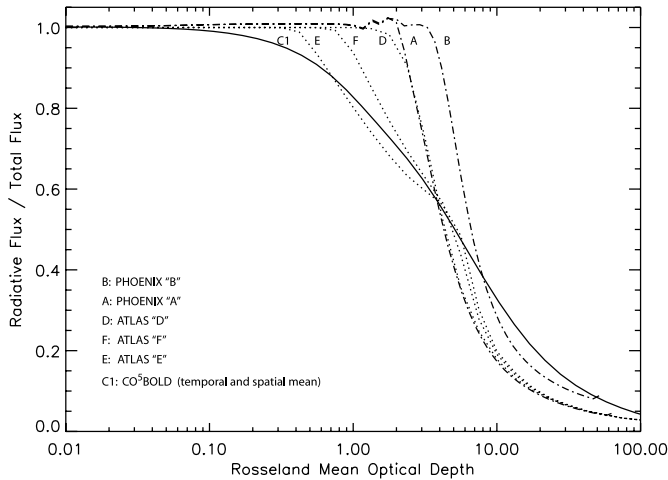| Parameter	Symbol	Value	Reference
Limb-darkened angular diameter (mas)	$\theta_{\rm LD}$	5.404 $\pm$ 0.031	Table 5, § 5
Bolometric flux (ergs cm^{-2} s^{-1})	$\mathcal{F}$	(17.86 $\pm$ 0.89) $\times$ 10^{-6}	§ 2.2
Effective temperature (K)....................................	$T_{\rm eff}$	6543 $\pm$ 84	$\theta_{\rm LD}$ and $\mathcal{F}$
Parallax (mas)	π	285.93 $\pm$ 0.88	Perryman et al. (1997)
Radius ($R_\odot$)..	R	2.031 $\pm$ 0.013	$\theta_{\rm LD}$ and π
Mass ($M_\odot$)...	M	1.42 $\pm$ 0.04	Girard et al. (2000)
Surface gravity (cm s^{-2})....................................	log g	3.975 $\pm$ 0.013	R and M

Fig. 8.—Comparison of the six model atmosphere radiative flux structures on a mean Rosseland optical depth scale: PHOENIX models A and B (*dash-dotted line*), ATLAS 12 models D, E, and F (*dotted line*), and CO⁵BOLD model C1 (*solid line*). The one-dimensional overshooting models E and F and the temporally and spatially averaged three-dimensional model C1 all have a significant fraction (5%–15%) of their total flux in convection at an optical depth of unity, while the other one-dimensional models are fully radiative at this depth.

cool supergiants. Instead, this effect must reside in the distribution of temperature with optical depth.

The best-fit angular diameter values presented in Table 5 and Figure 4 are quite insensitive to the model effective temperature. Fits obtained from a grid of PHOENIX models spanning a 2000 K range yield angular diameter differences of only 0.007, 0.006, and 0.004 mas at 500 nm, 800 nm, and 2.2 μm, respectively, values comparable to the formal fit uncertainties. The atmosphere models in Table 5 yield different angular diameters because they have different temperature gradients, as shown in Figure 7.

The mean temperature structure of the three-dimensional CO⁵BOLD model and the one-dimensional ATLAS 12 model F have shallower temperature gradients in the range $1 \leq \tau_{\rm Ross} \leq 5$ relative to the one-dimensional models without overshooting. This is expected because the radiative flux should be reduced when the convective flux is increased. Figure 8 shows the fraction of radiative flux as a function of optical depth for these models. The mean three-dimensional model and the one-dimensional model with overshooting have only ~80% of their total flux in radiation at $\tau_{\rm Ross} = 1$. At depths $\tau_{\rm Ross} \lesssim 8$, the mean three-dimensional and the one-dimensional overshooting radiative flux structures are quite similar. These best-fitting models to the interferometric data show significant convective flux at $\tau_{\rm Ross} \lesssim 1$, and we conclude that the interferometric data provide evidence for convective overshooting in Procyon's atmosphere.

The shallower temperature gradient introduced by overshooting reduces the relative LD between 500 nm and 2.2 μm. This accounts for the variation in the best-fit $\theta_{\rm LD}$ values for models with different convection treatments. An analysis of the contribution functions $S(\tau_\lambda)e^{-\tau_\lambda}$ at the three wavelengths shows that the 500 nm continuum forms in a range of depths partially below the depths forming the 800 nm continuum. The 800 nm band lies near the peak of the bound-free H⁻ opacity, the dominant continuum opacity in the optical. At 2.2 μm the H⁻ opacity, here free-free beyond the 1.6 μm H⁻ opacity minimum, is less than at 800 nm and similar to the 500 nm opacity. However, at 2.2 μm the intensity is much less sensitive to the temperature of Planckian radiation than at 500 nm. For the Sun, it was pointed out by Gingerich et al. (1971) that the lack of a steeply rising

Planck function (with temperature) at 1.6 μm means that the intensities emerging from the hot convective layers are better probed at wavelengths immediately to the red of the Balmer limit (365 nm), even if the optical depth is a factor of 2 larger there than at the 1.6 μm opacity minimum. In short, similar depths are probed by the 500 nm and 2.2 μm bands, but the radiation field is much more sensitive the temperature gradient at 500 nm compared to 2.2 μm.

One-dimensional models without overshooting cannot be made more consistent with the multiwavelength visibility data by adjusting the mixing-length parameter α. Based on the two stand-alone PHOENIX models A and B (see Table 5), changing α from 1.25 to 0.5 has no effect on the derived angular diameters at 800 nm and 2.2 μm. At 500 nm the two best-fit angular diameters differ by 0.35%. Note that model B with $\alpha = 0.5$ yields a slightly larger angular diameter at 500 nm relative to the $\alpha = 1.25$ model. Thus, reducing α slightly increases the degree of LD for a model that is already too limb darkened compared to the observations presented here.

5.3. *Photometry and One-dimensional Overshooting*

As discussed above, we find that the one-dimensional ATLAS 12 model F with 50% overshooting fits the visibility data as well as the three-dimensional CO⁵BOLD model and that the two models have similar mean temperature gradients. However, models with mixing-length theory convection and overshooting have been subject to extensive comparisons with photometry, with the results favoring models without overshooting (Castelli et al. 1997; Smalley & Kupka 1997). In general, one-dimensional convection treatments (e.g., mixing-length variants, turbulent convection) for model stellar atmospheres with otherwise identical parameters yield different SEDs. Strömgren photometric indices are often employed to facilitate the comparison of these different synthetic SEDs with a large number of real SEDs. Such studies (Heiter et al. 2002 and references therein) generally find that one-dimensional atmosphere models with no overshooting and $\alpha = 0.5$ more closely reproduce the colors of real atmospheres relative to other one-dimensional models. This is demonstrated for Procyon by Smalley & Kupka (1997), who show that to reproduce the observed $b - y$ index with an ATLAS 9 overshooting model requires a model with $T_{\rm eff} = 6830 \pm 142$ K (the uncertainly based on photometry alone), a value in excess of their derived interferometric value, $T_{\rm eff} = 6560 \pm 130$ K. This confirms the findings of Castelli et al. (1997). These results appear to be strengthened by our more precise value for the interferometric $T_{\rm eff}$ value, now 6543 ± 87 K, based on the mean K-band angular diameter value (see Table 7). Now the best-fit one-dimensional overshooting model to the photometry would appear to require a model $T_{\rm eff}$ value even more inconsistent with the interferometric $T_{\rm eff}$.

Heiter et al. (2002) find that reducing the mixing-length parameter α in ATLAS 9 models yields synthetic indices more consistent with observations. Our comparisons suggest that one-dimensional models with lower α-values better match photometry because this better approximates the composite SED in the b and v bands. As a result, constraining the one-dimensional α-parameter with Strömgren photometry most likely does not constrain the temperature structure of the one-dimensional model but instead reflects the lack of hotter temperature components in the one-dimensional model, the same components responsible for the continuum below 160 nm.

The composite SED models reproduce photometric indices quite close to the observed values and match fairly well the full UV continuum flux distribution. On the basis of the spatially

and temporally averaged three-dimensional radiative flux structure (Fig. 8), one might guess a much redder $b - y$ color for this model because of the similarity to ATLAS 12 model F. However, unlike the one-dimensional case, in the three-dimensional case the distribution of surface temperatures suppresses the one-to-one connection between the mean photospheric SED and the mean temperature structure. Both composite models predict $b - y$ values slightly redder than observed, but much more consistent than the one-dimensional overshooting models. A slightly warmer CO^{5}BOLD model ($T_{eff} = 6550$ instead of 6500 K), more consistent with the interferometric value 6543 K, is expected to yield a slightly warmer distribution of temperatures and hence a bluer $b - y$. A more consistent modeling approach, where the colors are computed directly from the three-dimensional model intensities, should clearly be pursued once the wavelength-dependent opacities in three-dimensional models improve.

6. SUMMARY

We find that the multiwavelength visibility measurements of Procyon obtained by the Mark III and the VLTI interferometers characterize the mean temperature structure of its atmosphere while UV and optical spectrophotometry characterize the spatial distribution of surface temperatures expected from granulation on its surface. We find that predictions from a three-dimensional CO^{5}BOLD hydrodynamic model atmosphere of Procyon match the interferometric, spectrophotometric, and photometric observations simultaneously, providing confidence in three-dimensional model predictions that until now had been tested predominantly with high-resolution spectroscopy. Based on three-dimensional and one-dimensional model comparisons, the interferometric data are consistent with a temperature structure with significant convective overshooting. While a one-dimensional model atmosphere with some overshooting matches the interferometric data, all one-dimensional models fail to match Procyon's SED, most evidently below 160 nm. Strömgren photometric indices appear to be sensitive to the multicomponent

brightness temperature distribution on Procyon's surface. This would seem to severely complicate conclusions regarding convection in similar stars based on one-dimensional model atmosphere comparisons to optical spectrophotometric data.

REFERENCES

Abe, F., et al. 2003, A&A, 411, L493
Allende Prieto, C., Asplund, M., López, R. J. G., & Lambert, D. L. 2002, ApJ, 567, 544
Anders, E., & Grevesse, N. 1989, Geochim. Cosmochim. Acta, 53, 197
Asplund, M., Grevesse, N., Sauval, A. J., Allende Prieto, C., & Kiselman, D. 2004, A&A, 417, 751
Asplund, M., Gustafsson, B., Kiselman, D., & Eriksson, K. 1997, A&A, 318, 521
Asplund, M., Nordlund, Å., & Trampedach, R. 1999, in ASP Conf. Ser. 173, Theory and Tests of Convection in Stellar Structure, ed. A. Giménez, E. F. Guinan, & B. Montesinos (San Francisco: ASP), 221
Baschek, B., Scholz, M., & Wehrse, R. 1991, A&A, 246, 374
Bessell, M. S., & Brett, J. M. 1988, PASP, 100, 1134
Bohlin, R. C. 1996, AJ, 111, 1743
Bohlin, R. C., & Gilliland, R. L. 2004, AJ, 127, 3508
Castelli, F., Gratton, R. G., & Kurucz, R. L. 1997, A&A, 318, 841
Chaboyer, B., Demarque, P., & Guenther, D. B. 1999, ApJ, 525, L41
Claret, A. 2000, A&A, 363, 1081
Code, A. D., Davis, J., Bless, R. C., & Hanbury Brown, R. 1976, ApJ, 203, 417
Cohen, M., Walker, R. G., Carter, B., Hammersley, P., Kidger, M., & Noguchi, K. 1999, AJ, 117, 1864
Crawford, D. L., & Barnes, J. V. 1970, AJ, 75, 978
Cunha, K., Smith, V. V., Boesgaard, A. M., & Lambert, D. L. 2000, ApJ, 530, 939
Davis, J., Tango, W. J., & Booth, A. J. 2000, MNRAS, 318, 387
Fields, D. L., et al. 2003, ApJ, 596, 1305
Freytag, B., Steffen, M., & Dorch, B. 2002, Astron. Nachr., 323, 213
Gingerich, O., Noyes, R. W., Kalkofen, W., & Cuny, Y. 1971, Sol. Phys., 18, 347
Girard, T. M., et al. 2000, AJ, 119, 2428
Glindemann, A., et al. 2003, Proc. SPIE, 4838, 89
Glushneva, I. N., Kharitonov, A. V., Kniazeva, L. N., & Shenavrin, V. I. 1992, A&AS, 92, 1
Gray, R. O., Napier, M. G., & Winkler, L. I. 2001, AJ, 121, 2148
Gustafsson, B., Bell, R. A., Eriksson, K., & Nordlund, A. 1975, A&A, 42, 407
Hanbury Brown, R., Davis, J., & Allen, L. R. 1974, MNRAS, 167, 121
Hauschildt, P. H., Allard, F., Ferguson, J., Baron, E., & Alexander, D. R. 1999, ApJ, 525, 871
Hauschildt, P. H., & Baron, E. 1999, J. Comput. Appl. Math., 109, 41
Heiter, U., et al. 2002, A&A, 392, 619
Johnson, H. L. 1965, Comm. Lunar Planet. Lab., 3, 73
Keenan, P. C. 1938, ApJ, 87, 45
Kervella, P., Ségransan, D., & Coudé du Foresto, V. 2004a, A&A, 425, 1161
Kervella, P., Thévenin, F., Morel, P., Berthomieu, G., Bordé, P., & Provost, J. 2004b, A&A, 413, 251
Kervella, P., Thévenin, F., Morel, P., Bordé, P., & Di Folco, E. 2003a, A&A, 408, 681
Kervella, P., et al. 2003b, Proc. SPIE, 4838, 858
Kiehling, R. 1987, A&AS, 69, 465
Koutchmy, S., Koutchmy, O., & Kotov, V. 1977, A&A, 59, 189
Kurucz, R. L. 1979, ApJS, 40, 1
———. 1992, Rev. Mex. AA, 23, 187
Lester, J. B., Gray, R. O., & Kurucz, R. L. 1986, ApJS, 61, 509
Ludwig, H.-G. 1992, Ph.D. thesis, Univ. Kiel
Ludwig, H.-G., Allard, F., & Hauschildt, P. H. 2002, A&A, 395, 99
Martić, M., et al. 1999, A&A, 351, 993
Matsushima, S. 1969, ApJ, 158, 1137
Matthews, J. M., Kusching, R., Guenther, D. B., Walker, G. A. H., Moffat, A. F. J., Rucinski, S. M., Sasselov, D., & Weiss, W. W. 2004, Nature, 430, 51
Mihalas, D. 1978, Stellar Atmospheres (2nd ed.; San Francisco: Freeman)
Milne, E. A. 1921, MNRAS, 81, 361
Morel, M., & Magnenat, P. 1978, A&AS, 34, 477

Mozurkewich, D., et al. 1991, AJ, 101, 2207
———. 2003, AJ, 126, 2502
Münch, G. 1945, ApJ, 102, 385
Neckel, H., & Labs, D. 1994, Sol. Phys., 153, 91
Nordström, B., et al. 2004, A&A, 418, 989
Ohishi, N., Nordgren, T. E., & Hutter, D. J. 2004, ApJ, 612, 463
Payne, C. H. 1925, Stellar Atmospheres (Harvard Obs. Monogr. 1; Cambridge: Harvard Obs.)
Perrin, G., Ridgway, S. T., Coudé du Foresto, V., Mennesson, B., Traub, W. A., & Lacasse, M. G. 2004, A&A, 418, 675
Perryman, M. A. C., et al. 1997, A&A, 323, L49
Plaskett, H. H. 1936, MNRAS, 96, 402
Robinson, F. J., Demarque, P., Li, L. H., Sofia, S., Kim, Y.-C., Chan, K. L., & Guenther, D. B. 2003, MNRAS, 340, 923
———. 2004, MNRAS, 347, 1208
Rodríguez-Pascual, P. M., González-Riestra, R., Schartel, N., & Wamsteker, W. 1999, A&AS, 139, 183
Schwarzschild, K. 1906, Göttingen Nachr., 195, 41 (English transl. in Selected Papers on the Transfer of Radiation, ed. D. H. Menzel [1966; New York: Dover])

Shao, M., Colavita, M. M., Hines, B. E., Staelin, D. H., & Hutter, D. J. 1988, A&A, 193, 357
Short, C. I., & Hauschildt, P. H. 2005, ApJ, 618, 926
Smalley, B., & Kupka, F. 1997, A&A, 328, 349
Spiegel, E. A. 1963, ApJ, 138, 216
Stein, R. F., & Nordlund, Å. 1998, ApJ, 499, 914
Strömgren, B. 1966, ARA&A, 4, 433
Swihart, T. L. 1956, ApJ, 123, 143
Travis, L. D., & Matsushima, S. 1968, ApJ, 154, 689
———. 1973, ApJ, 180, 975
Unsöld, A. 1930, Z. Astrophys., 1, 138
Vernazza, J. E., Avrett, E. H., & Loeser, R. 1976, ApJS, 30, 1
Wedemeyer, S., Freytag, B., Steffen, M., Ludwig, H.-G., & Holweger, H. 2004, A&A, 414, 1121
Wildt, R. 1939, ApJ, 90, 611
Wittkowski, M., Aufdenberg, J. P., & Kervella, P. 2004, A&A, 413, 711
Wood, B. E., Harper, G. M., Linsky, J. L., & Dempsey, R. C. 1996, ApJ, 458, 761
Woolley, R. V. D. R. 1941, MNRAS, 101, 52